Journal of Marine Research, 74, 43–69, 2016

Western North Pacific Integrated Physical-Biogeochemical Ocean Observation Experiment (INBOX): Part 1. Specifications and chronology of the S1-INBOX floats

by Ryuichiro Inoue[1,2], Toshio Suga[1,3], Shinya Kouketsu[1], Toshiyuki Kita[3], Shigeki Hosoda[1], Taiyo Kobayashi[1], Kanako Sato[1], Hiroyuki Nakajima[4], and Takeshi Kawano[1]

ABSTRACT

An interdisciplinary project called the Western North Pacific Integrated Physical-Biogeochemical Ocean Observation Experiment (INBOX) has been conducted since 2011. In the oligotrophic subtropics south of the Kuroshio Extension near biogeochemical mooring S1 (30° N, 145° E), 18 floats, each with a dissolved oxygen sensor, have been deployed in a 150 × 150 km square area. With the horizontal (30 km) and temporal (2 days) resolution of the data, we observed an upper ocean structure associated with mesoscale eddies and ocean responses to atmospheric forcing. The data set obtained from the S1-INBOX study was used to elucidate the impacts of physical processes on biogeochemical phenomena. This article is the first in a series of articles: specific information about the floats and a chronology of events are provided.

Keywords: profiling floats, dissolved oxygen, subtropical North Pacific Ocean, eddy, typhoon

1. Introduction

The goals of the Western North Pacific Integrated Physical-Biogeochemical Ocean Observation Experiment (INBOX) were to acquire physical-biogeochemical data with profiling floats and to quantify impacts of physical processes on biogeochemical phenomena. By testing an observational capability and evaluating a performance of profiling floats, INBOX is expected to contribute, along with Oxygen-Argo (Gruber et al. 2007) and Bio-Argo (Claustre et al. 2010), to the design and implementation of a sustainable global biogeochemical observing system. INBOX contains two components (Fig. 1), which were deployed near the Japan Agency for Marine-Earth Science and Technology (JAMSTEC) biogeochemical mooring

1. Research and Development Center for Global Change, Japan Agency for Marine-Earth Science and Technology (JAMSTEC), 2-15 Natsushima-cho, Yokosuka 237-0061, Japan.
2. Corresponding author: ***e-mail: rinoue@jamstec.go.jp***
3. Department of Geophysics, Graduate School of Science, Tohoku University, 6-3 Aramkai-aza-Aoba, Aoba-ku, Sendai, 980-8578, Japan.
4. Japan Marine Works Japan Ltd., 3-54-1 Oppama-higashi, Yokosuka, 237-0063, Japan.

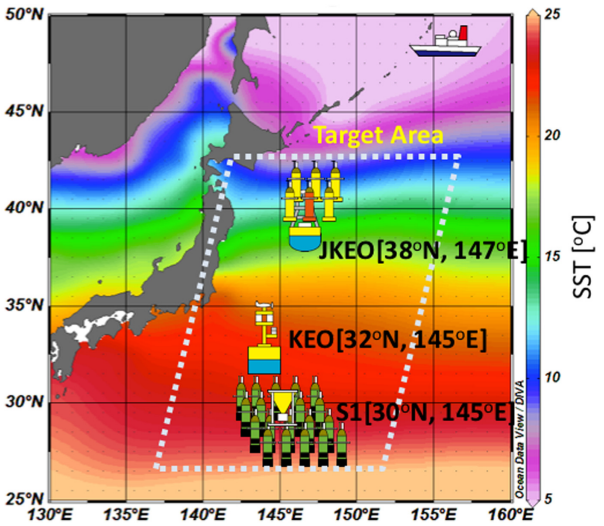

Figure 1. Schematic of Western North Pacific Integrated Physical-Biogeochemical Ocean Observation Experiment (INBOX). The color bar indicates the sea surface temperature (SST) scale. The trapezoid outlined by white dots represents the target area of INBOX. The SST is the annual mean from the *World Ocean Atlas 2005* (Locarnini et al. 2006). JKEO is the Japanese Kuroshio Extension Observatory mooring, KEO is the Kuroshio Extension Observatory mooring, and S1 is the biogeochemical mooring.

site S1 (Honda et al. 2013) and the Japanese Kuroshio Extension Observatory (Cronin et al. 2008; Tomita et al. 2010). This article will focus on the first component of INBOX (S1-INBOX), which has been deployed since July 2011 near the S1 mooring site (30° N, 145° E), located in the oligotrophic subtropical waters south of the Kuroshio Extension. We have been making use of data from the S1 mooring and shipboard measurements to interpret data acquired by the INBOX float array. The other component of INBOX has involved many floats intentionally trapped for approximately 2 years within a warm-core, anticyclonic eddy in the Kuroshio-Oyashio confluence zone (called ACE-INBOX), but it is not discussed here.

Although the surface layer (euphotic zone) of the North Pacific subtropical gyre is oligotrophic, because of its large area, it is thought to play an important role in oxygen production and carbon fixation through the net community production (e.g., Riser and Johnson 2008). However, the oligotrophic conditions in the gyre confound quantification of the mechanisms that supply nutrients to the surface layer, and hence, there is a need to quantify these fluxes (e.g., McGillicuddy et al. 1998). At the latitude of S1-INBOX, we expected that the confounding effects of the Kuroshio Extension, such as strong jets, meanders, and detached eddies, would be weak (e.g., Itoh and Yasuda 2010). Hence, it was hoped that we would be able to clarify the relationships between biogeochemical phenomena and physical processes, such as eddy-driven upwelling (e.g., McGillicuddy et al. 2007) and atmospheric

disturbances (e.g., Lin 2012). An important point to keep in mind is that the bottom of the euphotic zone at this latitude corresponds to the upper boundary of North Pacific Subtropical Mode Water (STMW), and properties and seasonal modulation of the STMW could therefore affect biogeochemical properties through lateral advection, nutrient recycling, and primary production in the euphotic zone (Palter, Lozier, and Barber 2005; Krémeur et al. 2009; Sukigara et al. 2011).

Eighteen profiling floats, each with a dissolved oxygen (DO) sensor, were deployed in a 150 × 150 km square area centered at the S1 mooring. The DO floats allowed us to study biogeochemical phenomena within the subsurface euphotic zone, to which physical processes in the subtropics intermittently supply nutrients, and within which a shallow oxygen maximum (SOM) forms. To the best of our knowledge, the spatial resolution of the S1-INBOX array of DO floats is the highest of any study aimed at elucidating the relationships between physical processes and biogeochemical phenomena in the subtropics. With a horizontal resolution of 30 km and temporal resolution of 2 days, we tried to evaluate impacts on biogeochemical processes of mesoscale eddies, which have horizontal scales of a hundred kilometers and temporal scales of several days to months. The uniqueness of the S1-INBOX experimental design and public availability of the data set (http://www.usgodae.org/argo/argo.html; http://www.coriolis.eu.org/) will greatly benefit the oceanographic community, especially scientists who design float experiments or who will use the S1-INBOX data set. This article gives an overview of S1-INBOX. In Section 2, we document the float specifications, and in Section 3 we describe the chronology of events such as eddies and atmospheric forcing that were observed by the S1-INBOX float array. The chronology of events is based on assignment of time intervals in days since 1 January 2011, and the time interval is identified by the year day number (YDAY = 0 at 1 January). This article references or is referenced in two other S1-INBOX articles (Inoue et al. [2016] and Kouketsu, Inoue, and Suga [2016], hereafter referred to as Part 2 and Part 3, respectively), which focused on a weak cyclonic eddy observed during S1-INBOX.

2. Float deployment and performance

In late July 2011, during the R/V *Mirai* cruise MR11-05, we launched 20 Navigating European Marine Observer (NEMO) floats (Optimare, Bremerhaven, Germany) and two Autonomous Profiling Explorer (APEX) floats (Teledyne Webb Research, Falmouth, MA) (Table 1 and technical information provided online at http://www.jamstec.go.jp/ARGO/inbox/s1/). Unfortunately, 4 of the total of 22 floats were broken during or immediately after launch as specified subsequently. Each float was equipped with an SBE41 or SBE41CP conductivity-temperature-depth (CTD) sensor (Sea-Bird Electronics Inc. [SBE], Bellevue, WA) and an Optode 3830 sensor (Aanderaa Data Instruments, Nesttun, Norway) to measure DO. Five shipboard CTD casts were conducted for calibration purposes when the floats were launched (Fig. 2). Each shipboard CTD was equipped with a RINKO (JFE Advantech, Nishinomiya, Japan) oxygen sensor, which is based on an optical (phosphorescence)

Table 1. Summary of the S1-INBOX floats: the float serial number (SN) and float type, World Meteorological Organization (WMO) number, launch date, launch position, profiling number on 5 August 2011 (change to 2-day profiling cycle), profiling number on 20 January 2012 (change to a profiling depth of 1,500 dbar), profiling number on 17 May 2012 (change to the Argo standard profiling cycle), and the last profiling number and date.

SN and float type	WMO number	Deployment date (2011)	Deployment position	Profile number on 5 August 2011	Profile number on 20 January 2012	Profile number on 17 May 2012	Date of the last communication (profile number)
199, NEMO	2902433	23 July	29.738° N, 144.945° E	8	92	151	19 October 2013 (#203)
168, NEMO	2902434	23 July	29.475° N, 145.000° E	8	—	—	5 May 2012 (#145; drifting on surface after #85)
193, NEMO	2902435	23 July	29.467° N, 145.298° E	8	92	151	16 July 2012 (#158)
4267, APEX	—	23 July	29.464° N, 145.595° E	7	—	—	28 January 2012 (#95; all data quality was bad)
194, NEMO	2902436	23 July	29.730° N, 145.599° E	8	—	139	13 November 2012 (#157)
196, NEMO	2902437	23 July	29.999° N, 145.600° E	8	92	151	16 June 2012 (#154; drifting on surface after #137)
195, NEMO	2902438	23 July	30.264° N, 145.600° E	8	92	151	16 July 2012 (#157)
197, NEMO	2902439	23 July	30.533° N, 145.599° E	8	92	151	5 August 2012 (#159)
201, NEMO	—	23 July	30.534° N, 145.302° E	—	—	—	23 July 2011 (antenna was broken)
202, NEMO	—	23 July	30.535° N, 145.003° E	—	—	—	23 July 2011 (never submerged)
198, NEMO	2902440	23 July	30.268° N, 145.000° E	8	—	—	13 April 2012 (#134)

(Continued)

Table 1. Continued

SN and float type	WMO number	Deployment date (2011)	Deployment position	Profile number on 5 August 2011	Profile number on 20 January 2012	Profile number on 17 May 2012	Date of the last communication (profile number)
162, NEMO	2902441	23 July	29.999° N, 144.410° E	8	92	151	18 December 2013 (#209)
161, NEMO	2902442	23 July	29.738° N, 144.401° E	8	92	151	24 October 2012 (#167)
200, NEMO	2902443	23 July	29.470° N, 144.400° E	8	92	151	11 July 2013 (#193)
164, NEMO	2902444	24 July	29.467° N, 144.698° E	8	92	—	17 May 2012 (#151)
4985, APEX	2902445	30 July	29.993° N, 145.004° E	4	—	147	7 January 2014 (#207)
170, NEMO	2902446	30 July	30.258° N, 145.294° E	3	87	146	3 November 2012 (#163)
169, NEMO	2902447	30 July	30.000° N, 145.299° E	3	87	146	8 November 2013 (#200)
167, NEMO	2902448	30 July	29.734° N, 145.291° E	3	87	146	8 November 2013 (#200)
166, NEMO	2902449	30 July	29.741° N, 144.694° E	4	88	146	4 October 2012 (#161)
163, NEMO	2902450	30 July	30.002° N, 144.700° E	3	—	146	16 June 2012 (#149; drifting on surface after #74)
165, NEMO	—	31 July	30.267° N, 144.700° E	3	—	146	16 June 2012 (#149; pressure sensor was broken)

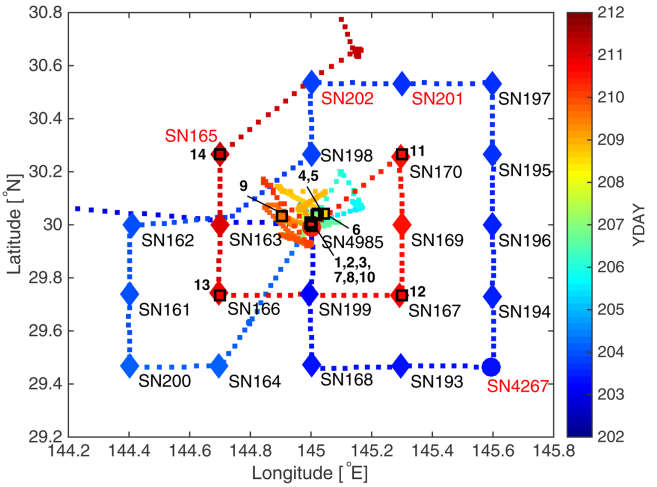

Figure 2. Ship tracks (colored squares), float launch positions (e.g., SN161), and conductivity-temperature-depth (CTD) stations (black open squares) during the deployment of S1-INBOX floats (#1–14). CTD casts at #10–14 were used for the calibration of the floats' dissolved oxygen sensors. Filled diamonds represent NEMO floats, and circles are APEX floats. Color bar shows the YDAY on the ship tracks. Floats broken just after the launches are shown in red letters. APEX, Autonomous Profiling Explorer; NEMO, Navigating European Marine Observer; SN, serial number; S1-INBOX, Western North Pacific Integrated Physical-Biogeochemical Ocean Observation Experiment conducted around the S1 biogeochemical mooring site; YDAY, year day number (time interval in days since 1 January 2011).

principle, and its response time is 1 second. The RINKO oxygen data were adjusted to oxygen concentrations in sample bottles measured by the Winkler method (Dickson 1996). The standard deviation of the difference between the adjusted RINKO oxygen data and the Winkler oxygen data was approximately 2 μmol kg^{-1}. Comparisons of the oxygen data from the first profile of DO floats and the RINKO data suggested that the DO values from the Optode 3830s were lower than the RINKO values by up to 30 μmol kg^{-1}. We then adjusted the oxygen data from the Optode 3830s by using the calibration equations proposed by Uchida et al. (2008). The calibration coefficients were modified by the quasi-Newton method to fit our observations. The calibration was made between the shipboard and float CTD data, which had the same potential temperature-salinity (θ-S) relation. The standard deviation of the difference between the adjusted oxygen data from the Optode 3830s and the RINKO data below 200 dbar, where temporal and spatial variability was relatively smaller than that near the sea surface, was 3.3 μmol kg^{-1}. This value was much smaller than the observed variability associated with a passage of eddies ($>$10 μmol kg^{-1}) described in this article. This technique for adjusting the DO sensor data was developed in our laboratory and has been prepared for publication (K. Sato, H. Uchida, S. Kouketsu, T. Suga, and S. Hosoda). The drift of DO sensors was examined by comparing observed DO values with saturated

DO values at 10 dbar where DO should be close to saturation. We found that the DO values measured by float serial number (SN) 164 continued to decrease below saturation after November (data not shown). This only occurred in float SN164 during the data period used in this article, and the DO data after 31 October from this float were discarded.

During S1-INBOX, floats drifted at 1,500 dbar (the parking depth of the float) and then descended to 2,000 dbar (the profiling depth). During an ascent from 2,000 dbar to the sea surface, the floats measured temperature, conductivity, pressure, and DO. The sampling layers of NEMO floats were 6 dbar, 10–200 dbar at 5 dbar intervals, 200–500 dbar at 10 dbar intervals, 500–1,000 dbar at 20 dbar intervals, 1,000–2,000 dbar at 50 dbar intervals, and 2,010 dbar. Those of APEX were surface, 6 dbar, 10–50 dbar at 5 dbar intervals, 50–350 dbar at 10 dbar intervals, 350–650 dbar at 25 dbar intervals, 650–1,500 dbar at 50 dbar intervals, and 1,500–2,000 dbar at 100 dbar intervals. The SBE41CP sensor on APEX floats had a high-resolution mode, which measured pressure, temperature, and salinity every 2 dbar from 2,000 dbar to the surface.

Each float stayed at the sea surface for less than 1 hour (the time-out period), during which time it transmitted data via the Iridium system. Finally, each float returned to the parking depth and repeated the same procedure.

The CTD sensor on an APEX float (SN4267) was broken, and the pressure sensor on a NEMO float (SN165) was also broken. The antenna of a NEMO float (SN201) was broken during its launch, and this float was lost. One NEMO float (SN202) drifted on the sea surface after its launch on 23 July 2011. The bladder cover of this float had come off at launch, and this weight loss may have prevented the float from sinking. We picked it up at 6:25 (UTC) on 31 July at 30.63° N, 145.15° E. Those float data were not used in this study.

The sampling intervals of the floats were not uniform just after the launches and were changed to every 2 days on 5 August via the two-way Iridium system. As shown in Table 1, the profiling depth for 13 floats was changed from 2,000 dbar to 1,500 dbar on 20 January 2012 because 13 of those floats had approached the Izu-Ogasawara ridge, and two of them (SN163 on 25 December 2011 and SN168 on 6 January 2012) hit the seafloor and then started to drift on the sea surface. After revising the profiling depth, another NEMO float (SN196) hit the seafloor on 15 April 2012 and then started to drift on the sea surface.

The profiling mode of the remaining 16 floats has been changed to be consistent with the International Argo Program; since 17 May 2012, the parking depth has been 1,000 dbar, and profiling to 2,000 dbar occurs every 10 days. The last float stopped working on 7 January 2014. A summary of float details including meta data is provided in Table 1.

3. Chronology of S1-INBOX floats

a. Eddies

The time series of 1/4° × 1/4° daily gridded sea surface height anomalies (SSHAs) from the Archiving, Validation, and Interpretation of Satellite Oceanographic data set (Ducet, Le Traon, and Reverdin, 2000) indicated that first a weak cyclonic eddy and then an anticyclonic

eddy passed by the S1 mooring (Fig. 3). On YDAY 205 (Fig. 3a), the floats were located in the northwestern quarter of the cyclonic eddy. As the cyclonic eddy propagated westward (e.g., YDAYs 230–286 in Fig. 3b–f), it passed over the floats. As the anticyclonic eddy approached the floats from the northeast, the cyclonic eddy disappeared around YDAY 306, and the floats were trapped in the anticyclonic eddy (e.g., YDAYs 286–334 in Fig. 3f–i). The anticyclonic eddy kept propagating to the west (YDAY 346 in Fig. 3j). Finally, the anticyclonic eddy had passed over the floats by late January 2012 (not shown).

Under the influence of eddies, all floats moved westward 5° in longitude and over a range of 2° in latitude during a period of approximately 120 days (Fig. 4). There were loops in the trajectories of floats trapped in eddies. Float SN168, the trajectory of which formed a loop (YDAY <270), recorded water with a high oxygen concentration ($\sim$230 μmol kg^{-1}) between 40 and 80 dbar (the SOM) inside the cyclonic eddy (Fig. 5). Oxygen concentrations in the SOM were occasionally higher than the saturation value, which suggested the oxygen production because of photosynthesis (e.g., Shulenberger and Reid 1981; Craig and Hayward 1987). High oxygen concentrations (220 μmol kg^{-1}) in the anticyclonic eddy were also found at depths of 150–450 dbar (around YDAY 300). In that case, seasonal mixed-layer deepening because of surface cooling started after roughly YDAY 310 (Fig. 5c) and reached to the SOM depth. Because the sea surface cooling and mixed-layer formation started to erode the SOM when the anticyclonic eddy passed over the float, the effects of the anticyclonic eddy (e.g., possible nutrients injection or extraction because of eddy-driven vertical motions) on the SOM were less apparent toward the end of 2011. Note that float SN168 in Figure 5 was trapped in and passed by the cyclonic (Fig. 3d) and anticyclonic eddies (Fig. 3g), respectively. Float SN200 (Fig. 6) deployed on the west side of the cyclonic eddy (Fig. 3a) was caught by the cyclonic eddy around YDAY 275 (Fig. 3e) and then escaped from the anticyclonic eddy (Figs. 3g–j and 4). The time series of the oxygen concentration (Fig. 6c) indicated that the concentration at the SOM was less saturated outside of the cyclonic eddy because the relatively thicker oversaturated layer and higher concentration at the SOM were observed around YDAY 280 when float SN200 was in the cyclonic eddy (Fig. 3d and f). Note that in Figures 5(b), 6(b), and 7(a), to determine the oxygen concentration at the SOM, the profile was interpolated to 1 dbar intervals by using the Akima spline method (Akima 1970), and the SOM was simply defined to be the maximum concentration measured above 110 dbar.

To address impacts of eddies on the SOM and relations between the SOM and mixed-layer depths during S1-INBOX, all profiles were averaged over every 7 days. Then, the averaged oxygen concentration was compared with the saturation value (Fig. 7). The mixed-layer depth was defined to be the depth at which the density became 0.03 kg m^{-3} greater than the density at the sea surface (defined to be the average density over the shallowest observed layer to at most 10 dbar; de Boyer Montégut et al. 2004). From the average time series, the oxygen concentration was larger when the floats observed the cyclonic eddy before YDAY 270. Then, it started to decrease when the floats observed the anticyclonic eddy. It was suggested that the oxygen concentration was slightly higher ($\sim$10 μmol kg^{-1})

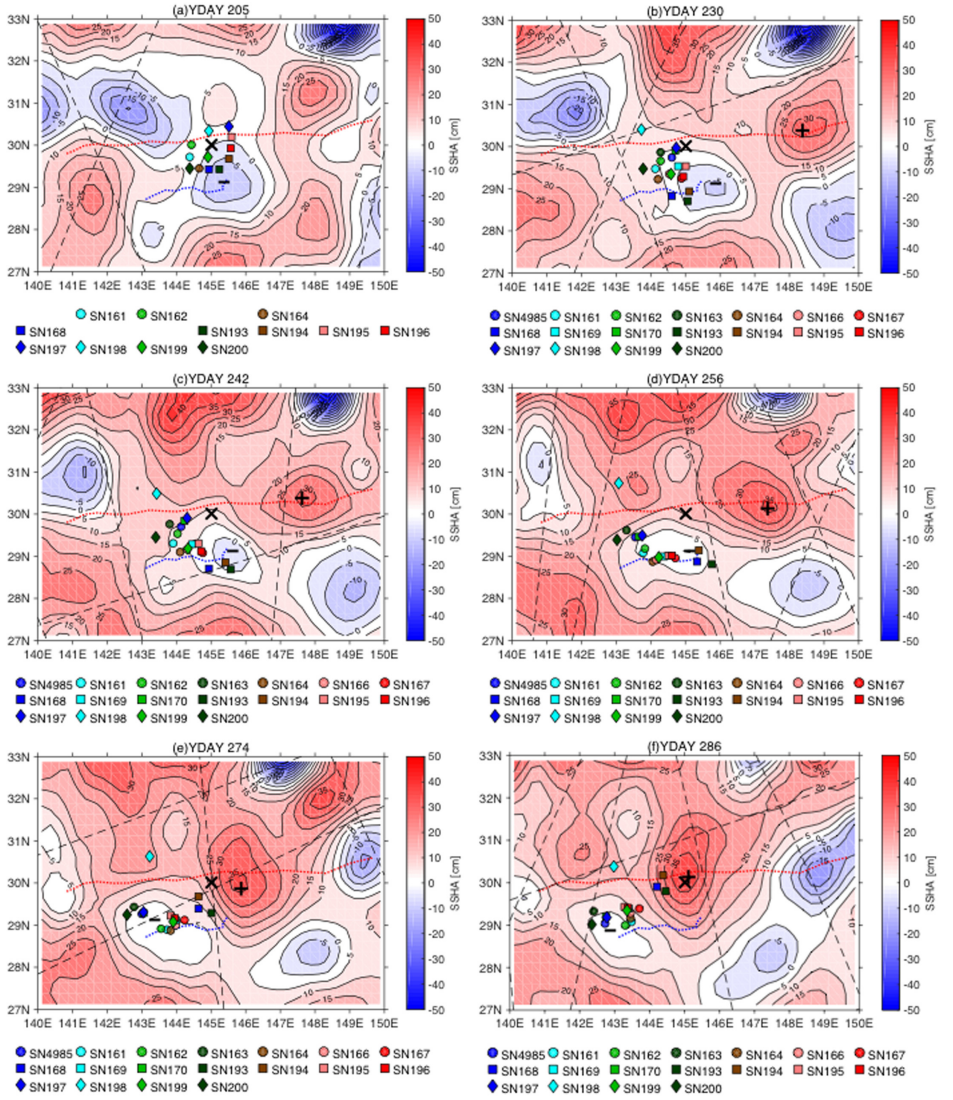

Figure 3. Sea surface height anomaly (SSHA) on (a) YDAY 205, (b) YDAY 230, (c) YDAY 242, (d) YDAY 256, (e) YDAY 274, (f) YDAY 286, (g) YDAY 306, (h) YDAY 318, (i) YDAY 334, and (j) YDAY 346. The color bar indicates the SSHA scale. Colored symbols show the positions of floats when they communicated with the data server. Dashed lines indicate the satellites' paths. Red and blue dotted lines are trajectories of the anticyclonic and cyclonic eddies, respectively, during the S1-INBOX period obtained from Chelton, Schlax, and Samelson (2011). The S1 mooring site is at 30° N and 145° E shown by the black X. The black minus and plus signs are centers of the cyclonic and anticyclonic eddies defined by the local SSHA minimum and maximum, respectively. Note that Typhoons MA-ON, TALAS, and SONCA passed nearby the S1-INBOX site on YDAYs 202, 241, and 260, respectively (Fig. 14). SN, serial number; S1-INBOX, Western North Pacific Integrated Physical-Biogeochemical Ocean Observation Experiment conducted around the S1 biogeochemical mooring site; YDAY, year day number (time interval in days since 1 January 2011).

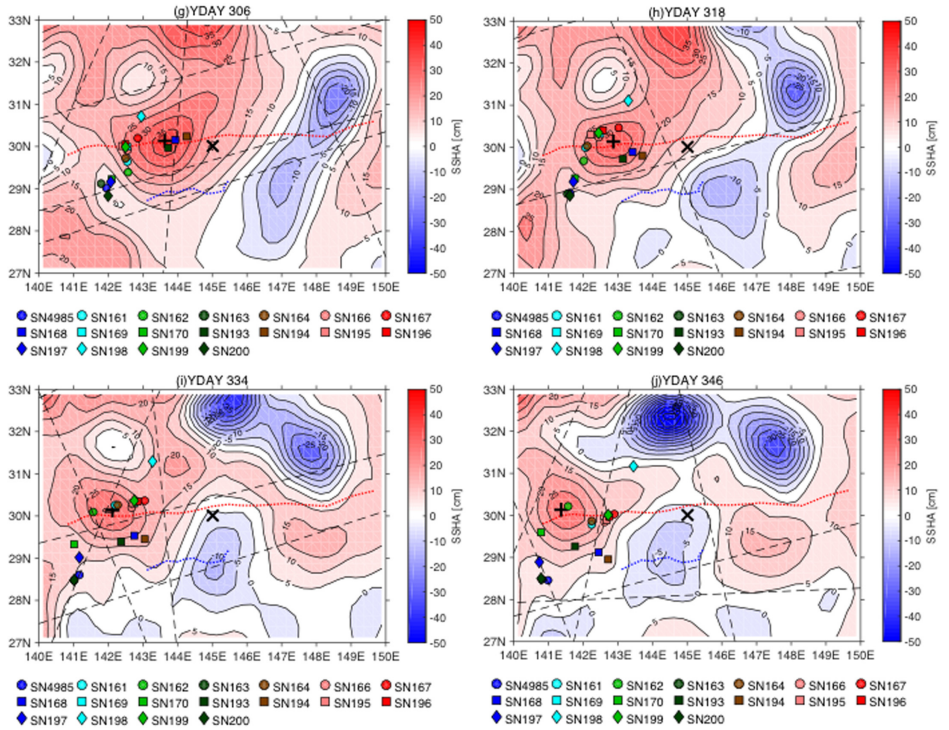

Figure 3. (Continued).

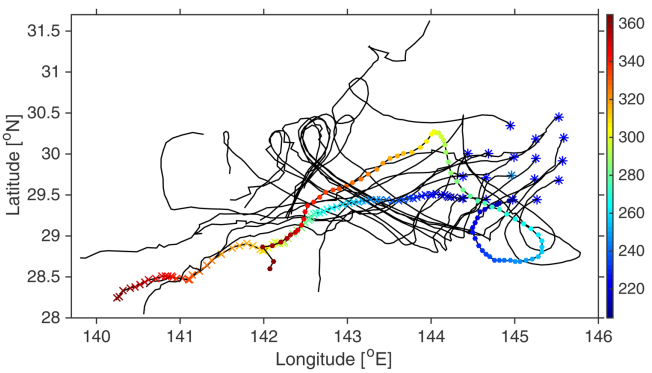

Figure 4. Trajectories of functional floats (Table 1) up to YDAY 364. Colored circles indicate the trajectory of SN168. Colored Xs indicate the trajectory of SN200. Here, color represents the YDAY shown in the color bar. Blue asterisks are the first-surfacing positions of floats after the launches. SN, serial number; YDAY, year day number (time interval in days since 1 January 2011).

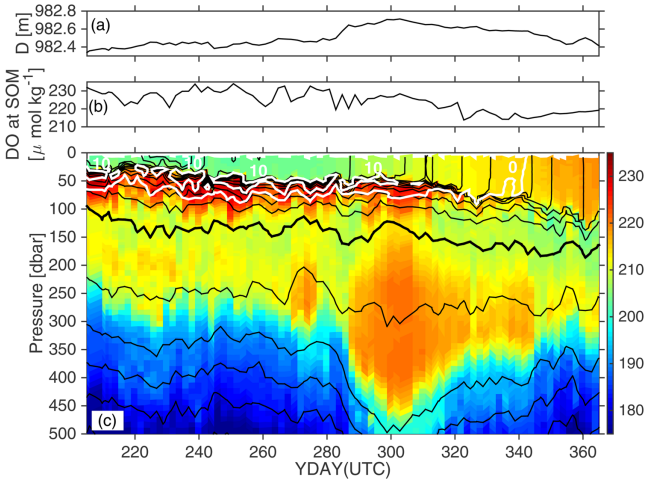

Figure 5. Time series of (a) dynamic height at 10 dbar relative to 1,000 dbar, $D = -\frac{1}{g}\int_{1,000}^{10} \frac{1}{\rho} dp$, where ρ is the in situ density. Time series of (b) dissolved oxygen (DO; μmol kg^{-1}) at the shallow oxygen maximum (SOM) and (c) vertical DO distribution recorded by float SN168. White contours in (c) show the difference between DO and the oxygen saturation concentration (Garcia and Gordon 1992). Positive values (oversaturated) are plotted with a contour interval of 10 μmol kg^{-1}. Contour lines show isopycnal surfaces, σ_θ (kg m^{-3}). The contour interval is 0.25 kg m^{-3}, and the thick line is $\sigma_\theta = 25$ kg m^{-3}, which is shown as a reference for the other contours. The color bar to the right indicates the DO scale. SN, serial number; YDAY, year day number (time interval in days since 1 January 2011).

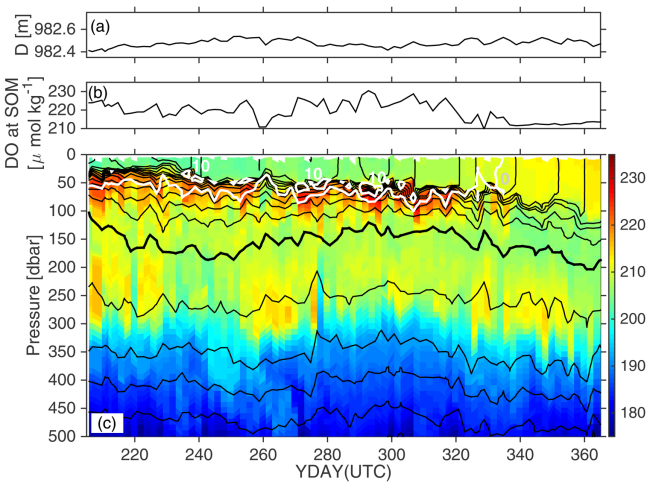

Figure 6. Time series of (a) dynamic height at 10 dbar relative to 1,000 dbar, (b) dissolved oxygen (DO; μmol kg^{-1}) at the shallow oxygen maximum (SOM), and (c) vertical DO distribution recorded by float SN200. Contours and the color bar in (c) are same as in Figure 5. SN, serial number; YDAY, year day number (time interval in days since 1 January 2011).

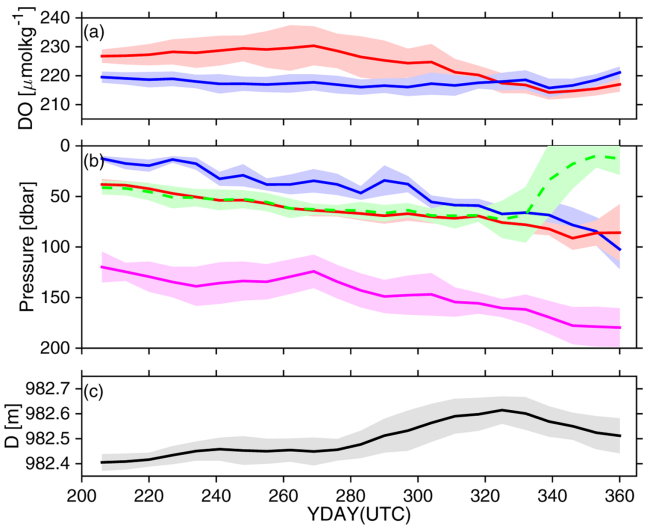

Figure 7. Time series of 7 days–averaged (a) dissolved oxygen (DO; μmol kg^{-1}, red line) and saturation value (blue) at the shallow oxygen maximum (SOM); (b) mixed-layer depth (blue), the SOM depth (green dashed), depth of the $\sigma_\theta = 24$ kg m^{-3} isopycnal surface (red), and $\sigma_\theta = 25$ kg m^{-3} isopycnal surface (magenta); and (c) dynamic height at 10 dbar relative to 1,000 dbar. Shadings indicate the standard deviations. All available floats were used. YDAY, year day number (time interval in days since 1 January 2011).

than the saturation value when the averaged SOM depth followed the averaged depth of $\sigma_\theta = 24$ kg m^{-3} isopycnal surface. Here σ_θ is potential density ρ_θ-1000 kg m^{-3}. The SOM was slightly undersaturated when the maximum oxygen concentration was observed within the mixed layer after YDAY 320 because of the wintertime mixed-layer deepening. Although the single float time series (Fig. 5) indicated the doming structure of the isopycnal surface of $\sigma_\theta = 25$ kg m^{-3} around YDAY 300, this tendency was not found in the averaged isopycnal surface depth possibly because of the floats' dispersion.

To examine an observed horizontal structure of eddies and that of the oxygen concentration, which could not be described with the averaged time series (Fig. 7), the oxygen concentrations at the SOM and isopycnal surface depths were plotted with respect to each eddy center (Figs. 8 and 9). Here, the eddy centers were determined from the minimum and maximum values of the SSHA during YDAY 204–290 and 214–364 within insides of the cyclonic and anticyclonic eddies (Fig. 3), respectively. These periods were determined from the experiment period (YDAY 204–364) and the eddy trajectories distributed by Chelton, Schlax, and Samelson (2011). The northwestern side of the cyclonic eddy was relatively well sampled (Fig. 8a) because of the deployment positions (Fig. 3a). The oxygen concentration at the SOM was highest near the eddy center and higher in northwestern part of the eddy (Fig. 8a and c). The standard deviation of the concentration (Fig. 8e) was low

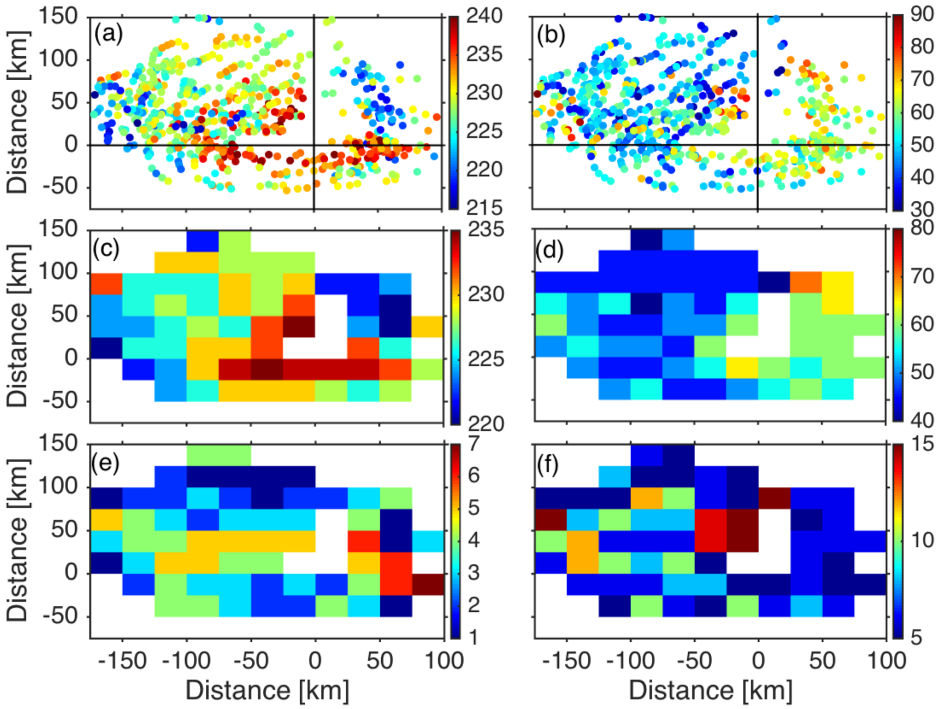

Figure 8. Horizontal distributions of properties relative to the cyclonic eddy center during YDAYs 204–290: (a) dissolved oxygen (DO; μmol kg^{-1}) at the shallow oxygen maximum (SOM), (b) the SOM depth (dbar), (c) bin average (25 $\times$ 25 km) of DO at the SOM, (d) bin average of the SOM depth, (e) standard deviation of DO at each bin, and (f) standard deviation of the SOM depth at each bin. The data bin, which includes data greater than or equal to 3, is shown. Values are indicated in the color bar on the right in each panel.

near the eddy center, but it was increased in the northwestern part even with large profiling numbers. This might indicate temporal and spatial variability of the SOM structure at the leading edge of the cyclonic eddy. Depths of the SOM (Fig. 8b and d) were shallower in the northwestern part but were deeper in the east. Because the eddy was decaying when floats observed the eastern part of the eddy, it was possible that the eddy center was not accurately defined by the SSHA minimum in this period (e.g., Fig. 3d). The anticyclonic eddy approached floats from the northeastern side. As a result, the southwestern part of the eddy was sampled first, and then the east side was sampled (Fig. 3f–h). During this period, the concentration (Fig. 9a) and the SOM depth (Fig. 9b) decreased because the mixed layer eroded the summertime SOM observed around 30–80 dbar (e.g., Figs. 5c and 6c). The depth of $\sigma_\theta = 25$ kg m^{-3} isopycnal surface became shallower near the eddy center (Fig. 9c) as seen in the single float time series (Fig. 5), which suggested the doming structure of the upper seasonal thermocline that characterizes the anticyclonic mode-water eddy (e.g.,

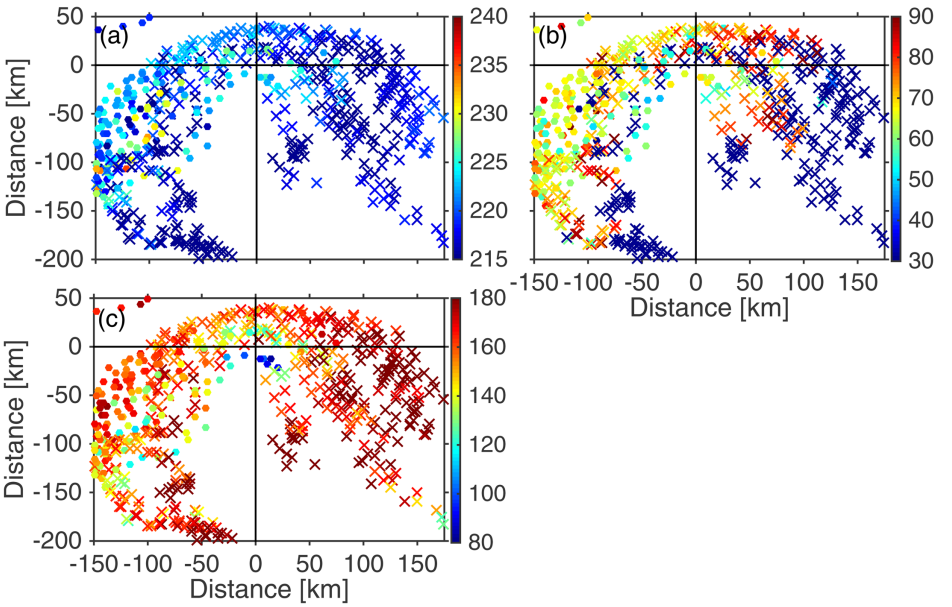

Figure 9. Horizontal distributions of properties relative to the anticyclonic eddy center: (a) dissolved oxygen (DO; μmol kg^{-1}) at the SOM, (b) the SOM depth (dbar), and (c) depth of $\sigma_\theta = 25$ kg m^{-3} isopycnal surface. Filled circles show profiles taken between YDAYs 214 and 309. The Xs show profiles taken between YDAYs 310 and 364. Values are indicated in the color bar on the right in each panel. YDAY, year day number (time interval in days since 1 January 2011).

McGillicuddy et al. 2007). However, it is not definitive because the deep mixed-layer formation because of the wintertime cooling could also deepen the isopycnal surface during the later observation period.

Because the property plot based on the eddy center was subject to the accuracy of the eddy center detection method and was expected to be less accurate for the weak eddy, the general features of the two eddies were further described by using composite plots (Figs. 10 and 12) and θ-S-DO diagrams (Figs. 11 and 13). To generate these plots, the SSHA values of the INBOX float profiles taken during YDAY 212–259 for the cyclonic eddy, where floats mainly stayed in the northwestern part before the eddy started to decay (Fig. 3a–d), and YDAY 304–333 for the anticyclonic eddy, where floats were trapped inside the eddy (Fig. 3g–i), within the region bounded by 140°–150° E, 27°–33° N were estimated, and profiles were bin averaged at 5 cm SSHA intervals. The vertically interpolated profiles explained previously were used for the bin averaging. In the cyclonic eddy (Fig. 10), the isopycnal surface shoaled, and salinity decreased toward the eddy center. The fact that oxygen (∼225 μmol kg^{-1}) was oversaturated at the SOM suggested that oxygen had been produced by photosynthesis. The θ-*S*-DO diagram (Fig. 11) confirmed that there was high-oxygen water with potential temperatures above 20°C and salinity between 34.7 and 34.75. There was

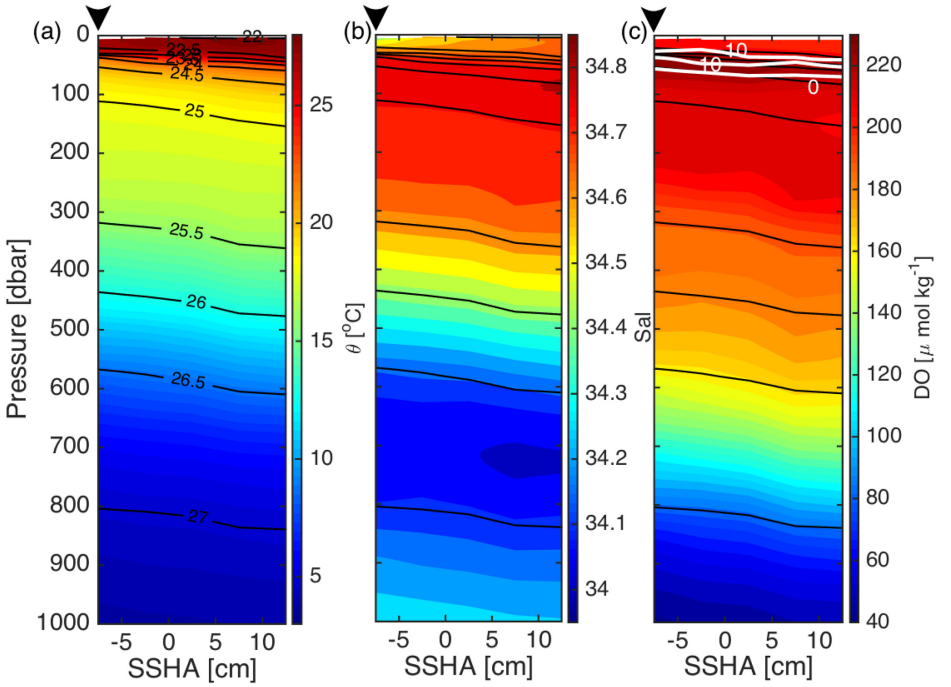

Figure 10. The composite mean structure of the cyclonic eddy: (a) potential temperature (°C), (b) salinity (Sal), and (c) dissolved oxygen (DO; μmol kg^{-1}). White contours in (c) show the difference between DO and the oxygen saturation concentration (Garcia and Gordon 1992). Positive values (oversaturated) are plotted with a contour interval of 10 μmol kg^{-1}. Black contour is σ_θ with a contour interval of 0.5 kg m^{-3}. Inverted triangle on the top indicates the eddy center. The bin −10 to −5 cm includes 6 profiles, −5 to 0 cm includes 103 profiles, 0 to 5 cm includes 250 profiles, 5 to 10 cm includes 104 profiles, and 10 to 15 cm includes 23 profiles. SSHA, sea surface height anomaly.

both high-salinity and low-salinity water at temperatures above 19°C, and the low-salinity water with DO as high as that of the previously mentioned high oxygen was observed. In the anticyclonic eddy (Fig. 12), near the eddy center, the potential temperature was uniform (17°C–18°C) and salinity was approximately 34.7 between $\sigma_\theta = 25$ and 25.5 kg m^{-3}, stratification was weak, and the isopycnal surface of $\sigma_\theta = 25$ kg m^{-3} shoaled toward the center of the eddy at the top of the homogeneous water at about 100 dbar, the indication being that this eddy contained STMW in its core and suggestive of a mode water eddy. There was a high-DO core (220 μmol kg^{-1}) in the region of 200–400 dbar that corresponded to the STMW core. This core was decoupled from the SOM (∼220 μmol kg^{-1}). Because this core was below the euphotic zone and the water was undersaturated with respect to oxygen, this high-oxygen STMW must have been formed during the previous winter and subducted/advected to the S1-INBOX site. Although it is reasonable to expect enhanced

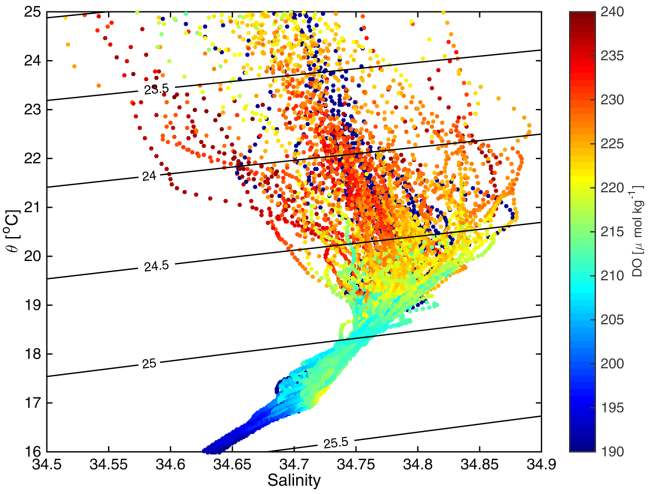

Figure 11. The θ-S-DO diagram obtained from DO floats within the cyclonic eddy. These float data were used to generate the composite mean structure of the cyclonic eddy (Fig. 10). Data corresponding to the sea surface height anomaly range of −10 to 0 cm were used. Color bar shows DO values (μmol kg^{-1}). The contour indicates σ_θ, and its interval is 0.5 kg m^{-3}. DO, dissolved oxygen.

production in a mode water eddy (McGillicuddy et al. 2007), the water was barely saturated with oxygen at the SOM (Fig. 12). However, this condition resulted in part from deepening of the mixed layer caused by seasonal surface cooling, as seen in Figures 5(c), 7(b), and 9(b). Similar double high-DO layers were also apparent in the θ-*S*-DO diagram (17°C–18°C and 21°C–23°C, respectively, in Fig. 13). Salinity was less scattered in the anticyclonic eddy than in the cyclonic eddy because the anticyclonic eddy was stable and isolated in the SSHA range (20–35 cm) associated with the data in Figure 13.

In summary, the floats observed a weak cyclonic eddy, which rapidly decayed during the observation period, but the SOM was oversaturated and less affected by the air–sea interactions because it was usually deeper than the mixed-layer depth. Then, the floats observed part of an anticyclonic eddy, which contained the STMW in the core, and that SOM was affected by the wintertime mixed-layer formation. If the SOM is not influenced by air–sea interactions, it should be governed by subsurface dynamics and local biogeochemical phenomena. We examine these relationships by analyzing the detailed structure of oxygen concentrations associated with the cyclonic eddy in Part3. We note that the anticyclonic eddy and winter mixed-layer formation have not been analyzed in this series of articles.

b. Typhoons

Typhoons are also known to cause dynamic responses of the ocean surface layer (e.g., Dickey et al. 1998; Sanford, Price, and Girton 2011) and enhance phytoplankton productivity

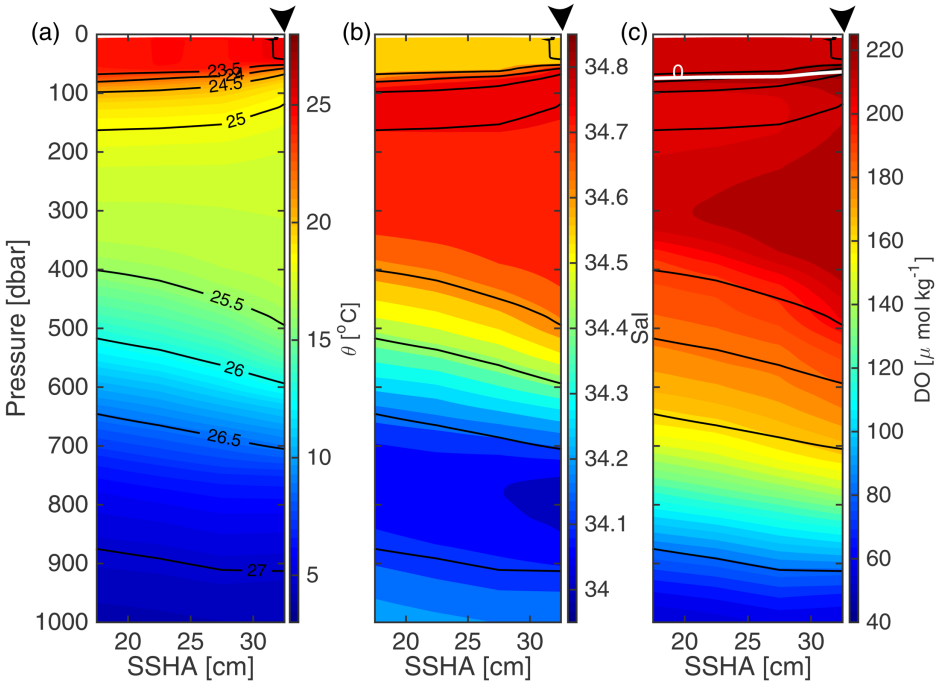

Figure 12. The composite mean structure of the anticyclonic eddy: (a) potential temperature (°C), (b) salinity (Sal), and (c) dissolved oxygen (DO; μmol kg^{-1}). Contours and symbols are the same as in Figure 10. The bin 30 to 35 cm includes 8 profiles, 25 to 30 cm includes 75 profiles, 20 to 25 cm includes 68 profiles, and 15 to 20 cm includes 27 profiles. SSHA, sea surface height anomaly.

(e.g., Lin et al. 2003; Shibano et al. 2011; Lin 2012). The responses could occur in several ways as a result of strong and localized wind forcing, during either the forced stage or the relaxation stage (e.g., Price 1981, 1983; Price, Sanford, and Forristall 1994). During the forced stage, deepening of the mixed layer and Ekman and inertial pumping are important for entrainment and upwelling, respectively, which bring deeper water to the surface. Suzuki, Niino, and Kimura (2011) summarized that Ekman pumping is dominant when $k \sim fLU^{-1} > 1$ (large and slow typhoons), where k is the nondimensional horizontal wavenumber of a typhoon, f is the Coriolis parameter, U is the moving speed of a typhoon, and L is the size of a typhoon. The inertial pumping is dominant when $k \sim fLU^{-1} \sim 1$ (under the resonant condition). The sea surface cooling was often observed and modeled in the right side of the typhoon track where the mixed-layer current resonated with winds that rotate clockwise and the entrainment was enhanced (e.g., Price 1981; Wada, Niino, and Nakano 2009). During the relaxation stage, near-inertial oscillations play an important role in transferring kinetic energy from the mixed layer into the thermocline and possibly in

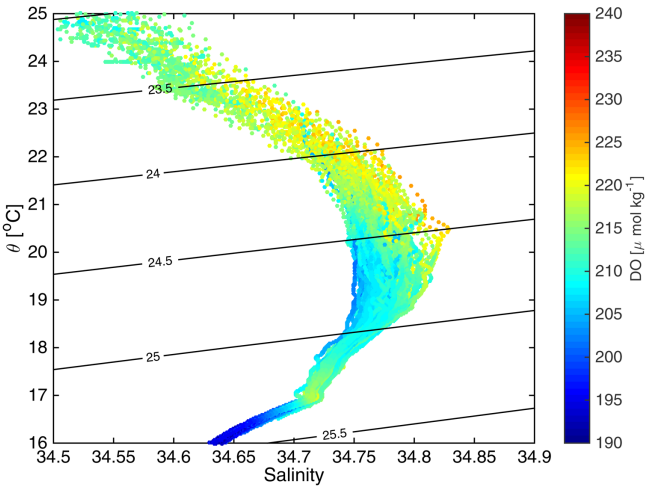

Figure 13. The θ-S-DO diagram obtained from DO floats within the anticyclonic eddy (Fig. 12). Data corresponding to the SSHA range 20 to 35 cm were used. The color bar and contour are the same as in Figure 11. DO, dissolved oxygen.

Table 2. Properties of typhoons. Typhoon data were obtained online from Japan Meteorological Agency (http://www.jma.go.jp/jma/jma-eng/jma-center/rsmc-hp-pub-eg/besttrack.html). Time is shown in UTC. STS, severe tropical storm; TY, typhoon.

		Minimum central pressure				
Typhoon name	Duration in YDAY (hour)	YDAY (hour)	Latitude (° N)	Longitude (° E)	Pressure (hPa)	Maximum wind (m s^{-1})
MA-ON (TY)	192 (0:00) to 204 (12:00)	196 (12:00)	21.9	137.1	935	49
TALAS (STS)	236 (0:00) to 247 (6:00)	240 (12:00)	24.1	140.1	970	26
SONCA (TY)	257 (6:00) to 262 (12:00)	261 (0:00)	34.6	144.3	970	36

deepening the mixed layer via shear instability at the base of the mixed layer (e.g., Sanford, Price, and Girton 2011).

Around the S1-INBOX period, three typhoons (MA-ON, TALAS, and SONCA in Tables 2 and 3) passed by the experiment site on YDAYs 202, 241, and 260, respectively. Typhoon MA-ON passed nearby the S1 mooring around YDAY 202, before the MR11-05 cruise (Fig. 14). It changed its course from southeastward to northeastward near the S1 mooring. The moderate resolution imaging spectroradiometer (MODIS) satellite (McClain, Feldman, and Hooker 2004; Feldman and McClain 2013) indicated increasing chlorophyll *a* concentrations after the passage of Typhoon MA-ON when S1-INBOX was started (Fig. 14a). Typhoon TALAS was a large, slow-moving typhoon, as is apparent in Table 3. The S1-INBOX site may have been affected around YDAY 241, when TALAS moved from the south toward the northwest. A westward wind blew for a few days (not shown). Although

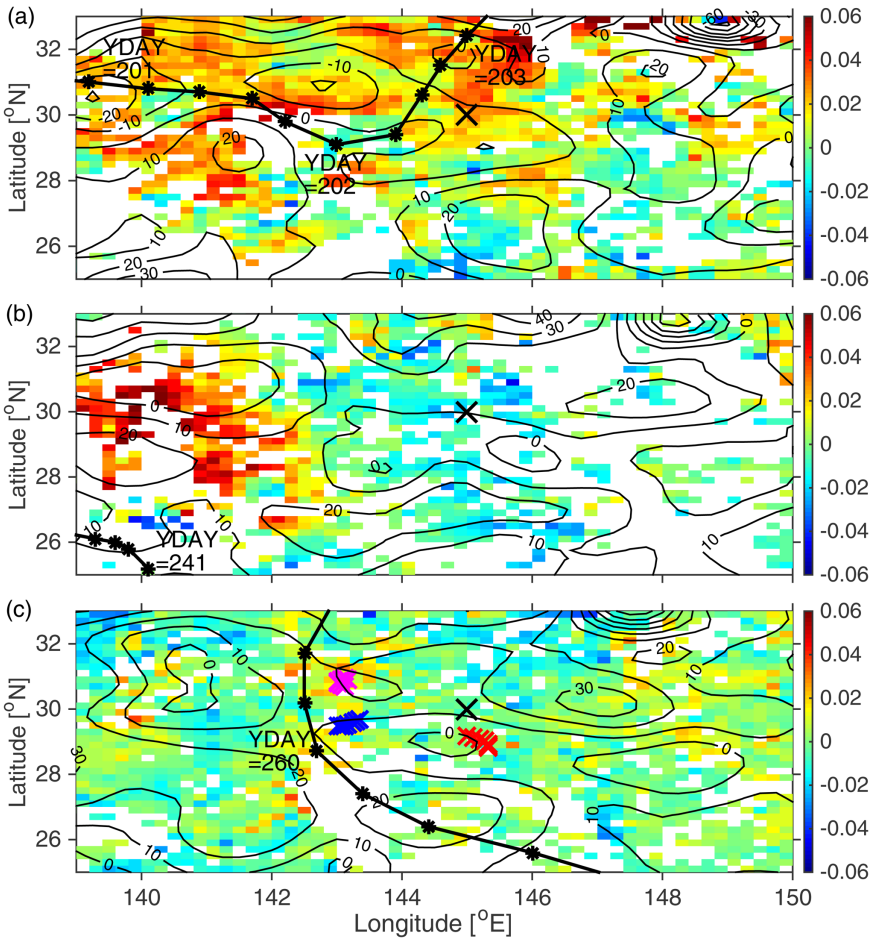

Figure 14. Average surface chlorophyll *a* difference (mg m^{-3}) from the MODIS satellite (McClain, Feldman, and Hooker 2004; Feldman and McClain 2013): (a) passage of Typhoon MA-ON (averaged over YDAYs 202–208 minus averaged over YDAYs 195–201, UTC), (b) passage of Typhoon TALAS (averaged over YDAYs 242–248 minus averaged over YDAYs 235–241), and (c) passage of Typhoon SONCA (averaged over YDAYs 260–266 minus averaged over YDAYs 253–259). The black X shows the S1 mooring site (30° N, 145° E). The black lines are typhoon trajectories. Black contour line shows weekly averaged sea surface height anomaly on the date of the typhoon event. The blue, red, and magenta Xs in (c) show locations of SN163, SN168, and SN198 between YDAYs 254 and 266, respectively. In each panel, color bar on right shows surface chlorophyll *a* difference between before and after the typhoon. MODIS, moderate resolution imaging spectroradiometer; SN, serial number; YDAY, year day number (time interval in days since 1 January 2011).

Table 3. Properties of typhoons at the location closest to the S1 mooring site. Typhoon data were obtained online from Japan Meteorological Agency (http://www.jma.go.jp/jma/jma-eng/jma-center/rsmc-hp-pub-eg/besttrack.html). Size indicates radius of winds >30 knots (15.4 m s^{-1}). Time is shown in UTC. STS, severe tropical storm; TS, tropical storm; TY, typhoon.

		Center position and central pressure						
Typhoon name	Arrival Time in YDAY (hour)	Latitude (° N)	Longitude (° E)	Pressure (hPa)	Maximum wind (m s^{-1})	Grade	Size (km)	Translation speed (m s^{-1})
MA-ON	202 (12:00)	30.6	144.3	990	23	TS	556	5.6
TALAS	241 (9:00)	26.0	139.6	970	26	STS	556	1.9
SONCA	260 (6:00)	30.2	142.5	975	33	TY	E: 370	7.7

both floats SN168 and SN200 observed the mixed-layer deepening (Figs. 5 and 6), this deepening only eroded part of the SOM and did not reach to the nutrient-rich water typically around the base of the euphotic zone. The MODIS satellite showed decreasing chlorophyll *a* concentrations around the S1-INBOX site after the passage (Fig. 14b). We conclude that the effect of TALAS around the S1-INBOX site was limited (Part2).

Typhoon SONCA was a fast-moving typhoon that passed to the west of the S1-INBOX site around YDAY 260 (Table 3), but the MODIS satellite showed no significant enhancement near the S1-INBOX site (Fig. 14c). Because some of the S1-INBOX floats were located closer to SONCA and took profiles every 2 days, we chose three profiling floats (SN163, SN168, and SN198) to elucidate the responses of the ocean to the passage of this typhoon. Float SN168 was located further east of the typhoon track in the cyclonic eddy around 29° N, 145.5° E; SN163 was just east of the track and in the eddy around 29.5° N, 143.25° E; and SN198 was just east of the track but outside of the eddy around 31° N, 143.25° E (Figs. 3d and 14c).

Because the inertial resonant condition approximately estimated from Table 3 indicated that the Ekman pumping was dominant under the typhoon track, the Ekman pumping velocity,

$$w_{Ek} = \frac{1}{\rho f}\left(\frac{\partial \tau_y}{\partial x} - \frac{\partial \tau_x}{\partial y}\right), \tag{1}$$

was calculated from hourly, 10 m wind speeds from the Japan Meteorological Agency forecast model (Saito et al. 2006; Saito 2012) at the locations of the three floats and used to diagnose responses of layers in the upper ocean. In equation (1), the parameter ρ is the surface density (1,022.3 kg m^{-3}), and f is the Coriolis frequency. The low-pass (at 1 cycle per day) filter was applied on the wind data. The parameters τ is the wind stress, calculated from the parameterization by Large and Pond (1981), and x and y represent the zonal and meridional directions, respectively.

Before and after the passage of Typhoon SONCA, DO at the SOM was high (~230 μmol kg^{-1}), and the water was oversaturated with O_2 to the east of the typhoon track

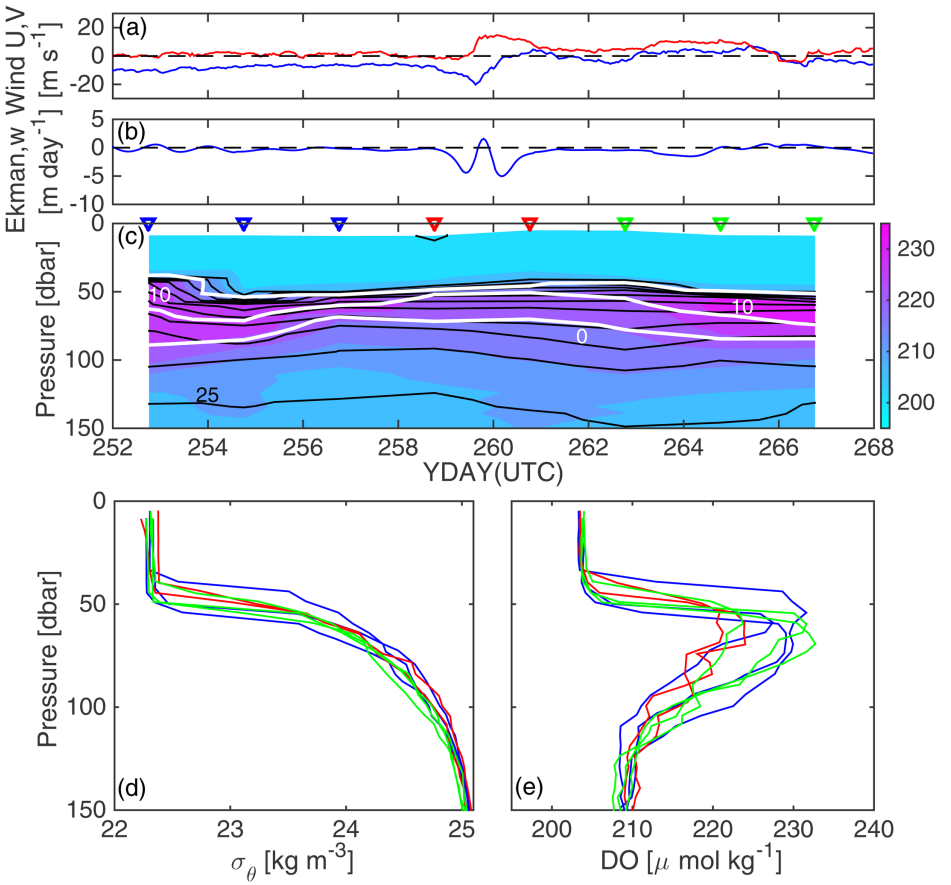

Figure 15. Time series of (a) hourly 10 m wind zonal (blue) and meridional (red) velocities at 29° N, 145.5° E (near the S1 mooring site) from the Japan Meteorological Agency forecast model (Saito et al. 2006; Saito 2012). (b) Ekman pumping vertical velocity and (c) vertical profiles of dissolved oxygen (DO; μmol kg^{-1}) from the float SN168. Black contour shows σ_θ (kg m^{-3}), and its interval is 0.25 kg m^{-3}. $\sigma_\theta = 25$ is shown as a reference. White thick contour is the difference between DO and saturation concentration for oxygen. Blue, red, and green inverted triangles show profiling dates before the passage of SONCA, just before and after the passage, and after the passage, respectively. Vertical profiles of (d) σ_θ and (e) DO. Line colors correspond to colors of the inverted triangles in (c), which represent the dates of profiling: blue is before the passage, red is just before and after the passage, and green is after the passage. SN, serial number; YDAY, year day number (time interval in days since 1 January 2011).

(SN168; Fig. 15). The implication is that oxygen had been produced by photosynthesis within the cyclonic eddy. During the passage of Typhoon SONCA, Ekman pumping velocity was relatively small (a few meters per day), and a homogeneous mixed layer was formed possibly because SN168 was located farther east of the typhoon track. DO values at the

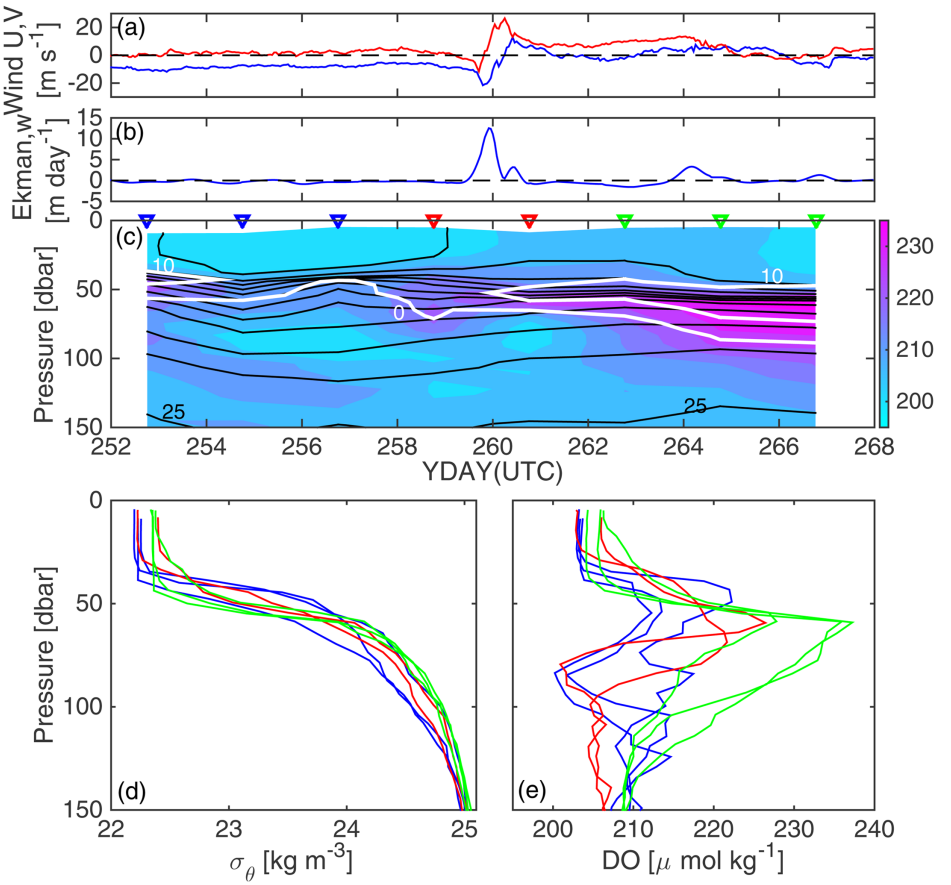

Figure 16. Time series of (a) hourly 10 m wind zonal (blue) and meridional (red) velocities, (b) Ekman pumping vertical velocity at 29.5° N, 143.25° E (near the typhoon track inside of the eddy), and (c) vertical profiles of dissolved oxygen (DO) from the float SN163. Vertical profiles of (d) σ_θ and (e) DO. Contour, symbols, and colors are the same as in Figure 15. SN, serial number; YDAY, year day number (time interval in days since 1 January 2011).

SOM decreased to ~220 μmol kg^{-1} (Fig. 15), and the O_2-oversaturated layer was thinned. Although we could not separate effects of horizontal advection with one float, this thinning indicated that vertical entrainment/mixing occurred during the passage of SONCA. Just to the east of the typhoon track but at the outer edge of the cyclonic eddy (SN163; Fig. 16), DO at the SOM increased to ~240 μmol kg^{-1}, and the water was oversaturated with O_2 after the passage of SONCA. During the passage of SONCA, a homogeneous mixed layer did not form, possibly because Ekman pumping was relatively strong, O (10 m day^{-1}) (e.g., Wada, Niino, and Nakano, 2009). Just to the east of the typhoon track but outside the eddy (SN198; Fig. 17), Ekman pumping was strongest, >30 m day^{-1}. Here again,

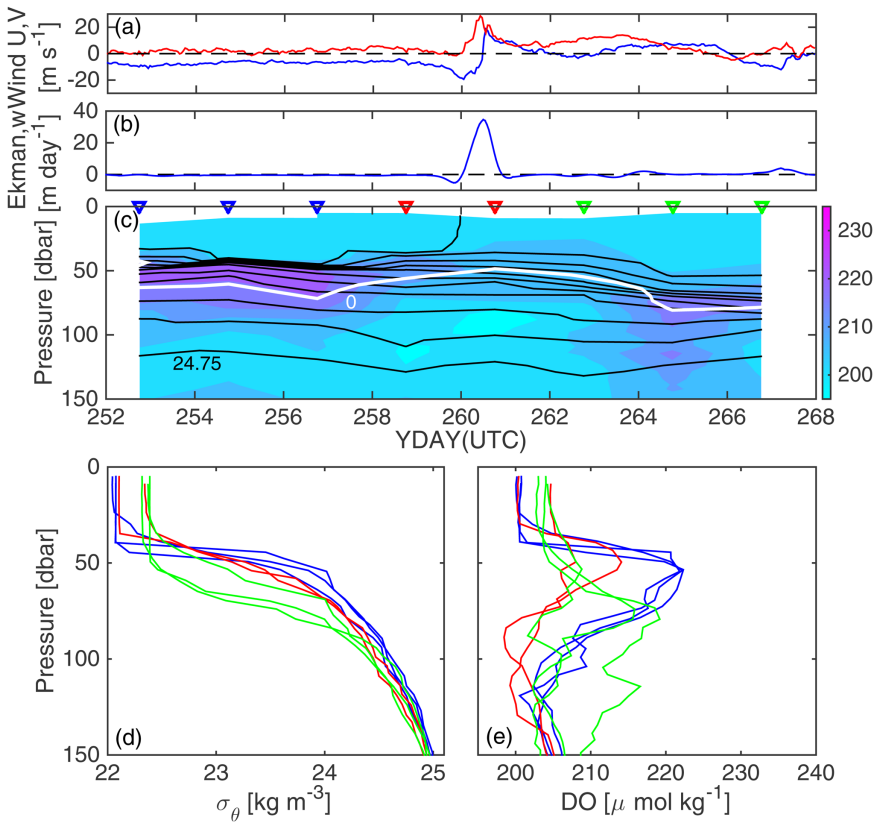

Figure 17. Time series of (a) hourly 10 m wind zonal (blue) and meridional (red) velocities, (b) Ekman pumping vertical velocity at 31° N, 143.25° E (near the typhoon track outside of the eddy), and (c) vertical profiles of dissolved oxygen (DO) from the float SN198. Vertical profiles of (d) σ_θ and (e) DO. Contour, symbols, and colors are the same as in Figure 15, but $\sigma_\theta = 24.75$ is shown as a reference in (c). SN, serial number; YDAY, year day number (time interval in days since 1 January 2011).

a homogeneous mixed layer did not form during the passage of SONCA but did form afterward. However, DO at the SOM was lower (~220 μmol kg^{-1} in Fig. 17) compared with the DO in the eddy, and the water was not oversaturated with O_2 after the passage of SONCA.

Although DO floats suggested that the typhoons could affect density and DO structures in the subsurface layers, the effect on biogeochemical phenomena near the S1 mooring site was less clear because surface chlorophyll *a* from the MODIS satellite was slightly enhanced only after the passage of MA-ON. Typhoon effects such as Ekman pumping and near-inertial motions on biogeochemical phenomena at 30° N, 145° E (at the S1 mooring site) are further examined in Part2.

4. Summary

We have introduced the S1-INBOX experiment, which was part of an interdisciplinary project called INBOX. The S1-INBOX was initiated in July 2011, and 18 floats, each with a DO sensor, were deployed in a 150 × 150 km square area centered at the S1 biogeochemical mooring (30° N, 145° E). We took advantage of the horizontal and temporal resolutions of 30 km and 2 days, respectively, to try to identify relationships between biogeochemical phenomena and physical processes, such as westward-propagating eddies and atmospheric disturbances.

We have provided specific information about the floats and described their chronology. Four floats out of the total of 22 floats were broken during or immediately after their launches. The last float stopped working on 7 January 2014. The floats were launched in the northwestern quarter of a weak cyclonic eddy. As the cyclonic eddy propagated westward, the floats recorded part of the decaying cyclonic eddy. As an anticyclonic eddy approached the floats from the northeast, the cyclonic eddy disappeared, and the floats were trapped in the anticyclonic eddy. The anticyclonic eddy continued to propagate to the west. By late January 2012, the anticyclonic eddy had passed over the floats. The floats recorded high oxygen concentrations at water depths of about 30–80 dbar (the SOM) inside the cyclonic eddy. The SOM depth was deeper than the mixed-layer depth suggesting it was less affected by the air–sea interactions. The oxygen concentration at the SOM was oversaturated. It was possible that oxygen was produced by photosynthesis, which could be influenced by subsurface dynamics. On the other hand, seasonal mixed-layer deepening because of surface cooling began when the floats were trapped in the anticyclonic eddy. Therefore, the SOM in the anticyclonic eddy was under the influence of air–sea interactions during the time that the floats were making measurements. There was a high DO concentration in the 200–400 dbar region. This region corresponded to the STMW core, which was decoupled from the SOM. We believe that it was formed during the previous winter and subducted/advected to the S1-INBOX site. During the S1-INBOX experiments, the mixed layer depth varied seasonally: it shoaled during the summer and deepened during the winter. Three typhoons passed by the S1-INBOX site just before and during the experiment, when the observational floats were in the cyclonic eddy. The data recorded by the S1-INBOX float array showed that a homogeneous mixed layer was not formed along the east side of the track of Typhoon SONCA during passage of the typhoon, and DO increased at the outer edge of the cyclonic eddy after passage of the typhoon. Further east of the typhoon track but inside the cyclonic eddy, a homogeneous mixed layer was formed during the passage of Typhoon SONCA, and DO increased after the typhoon had passed.

In subsequent articles (Part 2 and Part 3), influences of the cyclonic eddy and typhoons on the SOM variability were studied. Influences of the anticyclonic eddy and winter mixed-layer deepening on biogeochemical phenomena deserve further study.

Acknowledgments. We are indebted to the captain, crew, and other scientists on the R/V *Mirai* for their successful deployments of profiling floats. We thank Dr. Uchida at JAMSTEC for his help

for calibrations of floats' DO sensors and Mr. N. Matsuo at Marine Works Japan Ltd. for support on the float observations. Comments from reviewers greatly improved the manuscript. S. Kouketsu was supported by a Grant-in-Aid for Scientific Research on Innovative Areas (grant no. 12024485). The altimeter products were produced by Ssalto/Duacs and distributed by Archiving, Validation, and Interpretation of Satellite Oceanographic, with support from Centre National D'Etudes Spatiales Data Center (http://www.aviso.altimetry.fr/duacs/). We express our appreciation to Dr. M. Honda and the late Dr. Toshiro Saino at JAMSTEC for encouragement and fruitful discussions.

REFERENCES

Akima, H. 1970. A new method for interpolation and smooth curve fitting based on local procedures. J. Assoc. Comput. Mach., *17*(4), 589–602. doi: 10.1145/321607.321609

Chelton D. B., M. G. Schlax, and R. M. Samelson. 2011. Global observations of nonlinear mesoscale eddies. Prog. Oceanogr., *91*(2), 167–216. doi: 10.1016/j.pocean.2011.01.002

Claustre, H., J. Bishop, E. Boss, S. Bernard, J. F. Berthon, C. Coatanoan, K. Johnson, et al. 2010. Bio-optical profiling floats as new observational tools for biogeochemical and ecosystem studies: Potential synergies with ocean color remote sensing, *in* Proceedings of the OceanObs'09: Sustained Ocean Observations and Information for Society, Vol. 2, Venice, Italy, 21–25 September 2009, J. Hall, D. E. Harrison, and D. Stammer, eds. ESA Publication, WPP-306. Rome: European Space Agency.

Craig, H., and T. Hayward. 1987. Oxygen supersaturation in the ocean: Biological versus physical contributions. Science, *235*(4785), 199–202. doi: 10.1126/science.235.4785.199

Cronin, M. F., C. Meinig, C. L. Sabine, H. Ichikawa, and H. Tomita. 2008. Surface mooring network in the Kuroshio Extension. IEEE Syst. J., *2*(3), 424–430. doi: 10.1109/JSYST.2008.925982

de Boyer Montégut, C., G. Madec, A. S. Fischer, A. Lazar, and D. Iudicone. 2004. Mixed layer depth over the global ocean: An examination of profile data and a profile-based climatology. J. Geophys. Res.: Oceans, *109*, C12003. doi: 10.1029/2004JC002378

Dickey, T., D. Frye, J. McNeil, D. Manov, N. Nelson, D. Sigurdson, H. Jannasch, D. Siegel, T. Michaels, and R. Johnson. 1998. Upper-ocean temperature response to Hurricane Felix as measured by the Bermuda testbed mooring. Mon. Weather Rev., *126*, 1195–1201. doi: 10.1175/1520-0493(1998)126<1195:UOTRTH>2.0.CO;2

Dickson, A. G. 1996. Determination of dissolved oxygen in sea water by Winkler titration, in World Ocean Circulation Experiment (WOCE) Operations Manual. La Jolla, CA: WOCE Hydrographic Program Office. https://www.nodc.noaa.gov/woce/woce_v3/wocedata_1/whp/manuals/pdf/91_1/dickson2.pdf

Ducet, N., P. Y. Le Traon, and G. Reverdin. 2000. Global high-resolution mapping of ocean circulation from the combination of TOPEX/Poseidon and ERS-1 and -2. J. Geophys. Res.: Oceans, *105*(C8), 19477–19498. doi: 10.1029/2000JC900063

Feldman, G. C., and C. R. McClain. 2013. Ocean Color Web, MODIS Aqua, N. Kuring S. W. Bailey, eds. Greenbelt, MD: NASA Goddard Space Flight Center. http://oceancolor.gsfc.nasa.gov/

Garcia, H. E., and L. I. Gordon. 1992. Oxygen solubility in seawater: Better fitting equations. Limnol. Oceanogr., *37*(6), 1307–1312. doi: 10.4319/lo.1992.37.6.1307

Gruber, N., S. C. Doney, S. R. Emerson, D. Gilbert, T. Kobayashi, A. Körtzinger, G. C. Johnson, K. S. Johnson, S. C. Riser, and O. Ulloa. 2007. The Argo-Oxygen program, *in* Supporting Documents for the 8th Meeting of the International Argo Steering Team, Paris, France, 6–9 March 2007. Plouzane, France: Argo Information Center, 40–99.

Honda, M. C., H. Kawakami, S. Watanabe, and T. Saino. 2013. Concentration and vertical flux of Fukushima-derived radiocesium in sinking particles from two sites in the northwestern Pacific Ocean. Biogeosciences, *10*, 3525–3534. doi: 10.5194/bg-10-3525-2013.

Inoue, R., M. C. Honda, T. Fujiki, K. Matsumoto, S. Kouketsu, T. Suga, and T. Saino. 2016. Western North Pacific Integrated Physical-Biogeochemical Ocean Observation Experiment (INBOX): Part 2. Biogeochemical responses to eddies and typhoons revealed from the S1 mooring and shipboard measurements. J. Mar. Res., *74*(2), 71–99.

Itoh, S., and I. Yasuda. 2010. Characteristics of mesoscale eddies in the Kuroshio–Oyashio Extension region detected from the distribution of the sea surface height anomaly. J. Phys. Oceanogr., *40*(5), 1018–1034. doi: 10.1175/2009JPO4265.1

Kouketsu, S., R. Inoue, and T. Suga. 2016. Western North Pacific Integrated Physical-Biogeochemical Ocean Observation Experiment (INBOX): Part 3. Mesoscale variability of dissolved oxygen concentrations observed by multiple floats during S1-INBOX. J. Mar. Res., *74*(2), 101–131.

Krémeur, A.-S., M. Lévy, O. Aumont, and G. Reverdin. 2009. Impact of the subtropical mode water biogeochemical properties on primary production in the North Atlantic: New insights from an idealized model study. J. Geophys. Res.: Oceans, *114*, C07019. doi: 10.1029/2008JC005161

Large, W. G., and S. Pond. 1981. Open ocean momentum flux measurements in moderate to strong winds. J. Phys. Oceanogr., *11*, 324–336. doi: 10.1175/1520-0485(1981)011<0324:OOMFMI>2.0.CO;2

Lin, I., W. T. Liu, C.-C. Wu, G. T. F. Wong, C. Hu, Z. Chen, W.-D. Liang, Y. Yang, and K.-K. Liu. 2003. New evidence for enhanced ocean primary production triggered by tropical cyclone. Geophys. Res. Lett., *30*(13), 1718. doi: 10.1029/2003GL017141

Lin, I.-I. 2012. Typhoon-induced phytoplankton blooms and primary productivity increase in the western North Pacific subtropical ocean. J. Geophys. Res.: Oceans, *117*, C03039. doi: 10.1029/2011JC007626

Locarnini, R. A., A. V. Mishonov, J. I. Antonov, T. P. Boyer, and H. E. Garcia. 2006. World Ocean Atlas 2005, Vol. 1, Temperature, S. Levitus, ed. NOAA Atlas NESDIS 61. Washington, DC: U.S. Government Printing Office, 182 pp.

McClain, C. R., G. C. Feldman, and S. B. Hooker. 2004. An overview of the SeaWiFS project and strategies for producing a climate research quality global ocean bio-optical time series. Deep Sea Res., Part II, *51*(1–3), 5–42. doi: 10.1016/j.dsr2.2003.11.001

McGillicuddy, D. J., Jr., L. A. Anderson, N. R. Bates, T. Bibby, K. O. Buesseler, C. A. Carlson, C. S. Davis, et al. 2007. Eddy/wind interactions stimulate extraordinary mid-ocean plankton blooms. Science, *316*(5827), 1021–1026. doi: 10.1126/science.1136256

McGillicuddy, D. J., Jr., A. R. Robinson, D. A. Siegel, H. W. Jannasch, R. Johnson, T. D. Dickey, J. McNeil, A. F. Michaels, and A. H. Knap. 1998. Influence of mesoscale eddies on new production in the Sargasso Sea. Nature, *394*(6690), 263–266. doi: 10.1038/28367

Palter, J. B., M. S. Lozier, and R. T. Barber. 2005. The effect of advection on the nutrient reservoir in the North Atlantic subtropical gyre. Nature, *437*, 687–692. doi: 10.1038/nature03969

Price, J. F. 1981. Upper ocean response to a hurricane. J. Phys. Oceanogr., *11*, 153–175. doi: 10.1175/1520-0485(1981)011<0153:UORTAH>2.0.CO;2

Price, J. F. 1983. Internal wave wake of a moving storm. Part I: Scales, energy budget and observations. J. Phys. Oceanogr., *13*, 949–965. doi: 10.1175/1520-0485(1983)013<0949:IWWOAM>2.0.CO;2

Price, J. F., T. B. Sanford, and G. Z. Forristall. 1994. Forced stage response to a moving hurricane. J. Phys. Oceanogr., *24*, 233–260. doi: 10.1175/1520-0485(1994)024<0233:FSRTAM>2.0.CO;2

Riser, S. C., and K. S. Johnson. 2008. Net production of oxygen in the subtropical ocean. Nature, *451*, 323–325. doi: 10.1038/nature06441

Saito, K. 2012. The JMA nonhydrostatic model and its application to operation and research, *in* Atmospheric Model Applications, I. Yucel, ed. Rijeka, Croatia: InTech, pp. 85–110.

Saito, K., T. Fujita, Y. Yamada, J.-I. Ishida, Y. Kumagi, K. Aranami, S. Ohmori, et al. 2006. The operational JMA nonhydrostatic mesoscale model. Mon. Weather Rev., *134*, 1266–1298. doi: http://dx.doi.org/10.1175/MWR3120.1

Sanford, T. B., J. F. Price, and J. B. Girton. 2011. Upper-ocean response to Hurricane Frances (2004) observed by profiling EM-APEX floats. J. Phys. Oceanogr., *41*, 1041–1056. doi: http://dx.doi.org/10.1175/2010JPO4313.1

Shibano, R., Y. Yamanaka, N. Okada, T. Chuda, S. Suzuki, H. Niino, and M. Toratani. 2011. Responses of marine ecosystem to typhoon passages in the western subtropical North Pacific. Geophys. Res. Lett., *38*, LI8608. doi: 10.1029/2011gl048717

Shulenberger, E., and J. L. Reid. 1981. The Pacific shallow oxygen maximum, deep chlorophyll maximum, and primary productivity, reconsidered. Deep-Sea Res., Part A, *28*(9), 901–919. doi: 10.1016/0198-0149(81)90009-1

Sukigara, C., T. Suga, T. Saino, K. Toyama, D. Yanagimoto, K. Hanawa, and N. Shikama. 2011. Biogeochemical evidence of large diapycnal diffusivity associated with the subtropical mode water of the North Pacific. J. Oceanogr., *67*(1), 77–85. doi: 10.1007/s10872-011-0008-5

Suzuki, S., H. Niino, and R. Kimura 2011. The mechanism of upper-oceanic vertical motions forced by a moving typhoon. Fluid Dyn. Res., *43*(2), 025504. doi: 10.1088/0169-5983/43/2/025504

Tomita, H., M. Kubota, M. F. Cronin, S. Iwasaki, M. Konda, and H. Ichikawa. 2010. An assessment of surface heat fluxes from J-OFURO2 at the KEO and JKEO sites. J. Geophys. Res., *115*, C03018. doi: 10.1029/2009jc005545

Uchida, H., T. Kawano, I. Kaneko, and M. Fukasawa. 2008. In situ calibration of optode-based oxygen sensors. J. Atmos. Oceanic Technol., *25*(12), 2271–2281. doi: 10.1175/2008JTECHO549.1

Wada, A., H. Niino, and H. Nakano. 2009. Roles of vertical turbulent mixing in the ocean response to Typhoon Rex (1998). J. Oceanogr., *65*(3), 373–396. doi: 10.1007/s10872-009-0034-8

Received: *14 November 2013*; revised: *18 May 2015*.